RSC Advances

ROYAL SOCIETY OF CHEMISTRY

www.rsc.org/advances

The uniformly dispersed Bi closely contacted with bismuth tungastste can enhance the photocatalytic efficiency of bismuth tungastste.

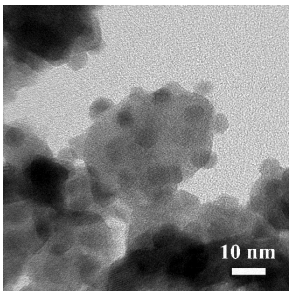

Journal Name

ARTICLE

In Situ Synthesis and Excellent Photocatalytic activity of tiny Bi Decorated Bismuth tungstate nanorods

Received 00th January 20xx,
Accepted 00th January 20xx

DOI: 10.1039/x0xx00000x

www.rsc.org/

Shi-Yu Lu, Ya-Nan Yu, Shu-Juan Bao* and Sheng-hui Liao

In this feature work, unique Bi/Bismuth tungstate nanocomposites were fabricated by an in situ one step hydrothermal reaction by using ethylene glycol as solvent. It is interesting to discover that not only morphologies but also composition of the products could be tailored by only adjusting the reaction temperature. When reaction temperature was below 220 °C, obviously shape evolution, from irregular nanoparticle aggregations, hollow spheres to small nanorods, were observed with the increasing of temperature; while when temperature was higher than 220 °C, not new morphology but also new phase, metal Bi appeared. In the as-prepared Bi/Bismuth tungstate nanocomposites, very tiny metal Bi formed in in situ reaction dispersed very well on the surface of bismuth tungstate nanorods, which make it exhibited excellent photocatalytic efficiency for the degradation of Rhodamine 6G (R6G). These results motivated us to perform a series of experiments to understand the forming mechanism and explore physic-chemical insight while providing guidance to prepare novel metal/Aurivillius oxide nanocomposites for photocatalytic performance.

Introduction

Currently, the world is facing formidable challenges in meeting rising requirement to clean environment. Persistent organic pollutants, heavy metals, etc. pollutants in water and soil are the key factors which make the environment worse and even trace pollutants enter human body will harm to human health.[1] Semiconductor-based heterogeneous photocatalysis represents an important scientific field due to its potential technological applications to solve above environmental issues and have been witnessed by numerous studies in recent years.[2] TiO_2 is the most efficient photocatalysis and most commercialized for widespread environmental applications such as remediation of hazardous wastes and contaminated groundwaters, control of toxic air contaminants, removal of toxic dyes from the industrial effluents, photo splitting of water, and cleanup of oil spills.[3-5] However, it can be only excited by ultraviolet irradiation and its absorption spectrum can only overlap a little part of solar spectrum.[6] In order to effectively utilize solar energy in photocatalytic processes, some solar-light-driven photocatalysts, such as bismuth-based Aurivillius oxide has received great interest in more recent years. Bi_2WO_6 is the simplest layered Aurivillius oxide with a narrow width of band gap (2.69 eV), which can be excited by visible light. Hence, it could be used as photocatalysts in water splitting and degradation of organic contaminants under solar light.[7] It is composed of perovskite-like $[WO_4]^{2-}$ layers sandwiched between bismuth oxide $[Bi_2O_2]^{2+}$ layers.[8] Such structure favors the efficient separation of photogenerated electron-hole pairs and then improves the photocatalytic activity due to the formed internal electric fields between the slabs.[9]

After the first report to synthesize Bi_2WO_6 nanostructure in hydrothermal process, hydrothermal method has been attracted more attention in fabricating Bi_2WO_6 and copious nano-architectured Bi_2WO_6 including nanofibers,[10] hollow tubes,[11] nanoplates,[12] micro-discs,[13] nanoflowers,[8, 14-16] hollow spheres[17-19] and inverse opals[20] have been constructed by tuning the experimental parameters (e.g., the precursor, reaction temperature, pH value, solvent or surfactant).[9, 14, 21-27] Up to now, a great deal of effort still focused on the morphology-controlled fabrication and photocatalytic properties of this material with hierarchical nanostructures.[22, 27,28] Then how to control the composition and crystal phase of the products by only adjusting the experimental parameters was still not been concerned.

Herein, a kind of low cost metal Bi-functionalized bismuth tungstate nanocomposites were fabricated in the first time by using ethylene glycol as solvent, the obtained metal Bi decorated bismuth tungstate with a small specific surface area (30 m^2g^{-1}) exhibited excellent photocatalytic efficiency for the degradation of R6G, which is much higher than that of pure Bi_2WO_6 hollow spheres with a high specific surface area (102 $m^2\ g^{-1}$). This result indicated that very tiny metal Bi uniformly distributed and closely contacted with bismuth tungastste nanorods play an important role in enhancing the photocatalytic efficiency of bismuth tungstate, which motivated us to perform a series of experiments to understand the forming mechanism and explore photocatalytic performance of the as-prepared materials.

Institute for Clean Energy & Advanced Materials, Faculty of Materials and Energy, Southwest University, Chongqing, 400715, P. R. China. E-mail: baoshj@swu.edu.cn

† Electronic supplementary information (ESI) available. See DOI:

Experimental Section

Bi/Bismuth tungstate nanocomposites

The samples were prepared by a typical hydrothermal process. $Bi(NO_3)_3 \bullet 5H_2O$ (3.477 mmol) and $Na_2WO_4 \bullet 2H_2O$ (1.740 mmol) were dissolved in 15 mL ethylene glycol (EG) under magnetic stirring, respectively. After the above solutions became clear, dropping Na_2WO_4 solution into the $Bi(NO_3)_3$ solution under stirring till to form clear solution. And then transform the resulting solution into a 50 mL Teflon-lined stainless steel autoclave. The autoclave was kept at different temperature for 20 h. Subsequently, the autoclave was cooled to room temperature naturally. The obtained samples were centrifuged, washed with distilled water and dried at 80 °C overnight. The samples obtained at different temperature (120 °C, 140 °C, 160 °C, 180 °C, 200 °C, 220 °C, 240 °C) were assigned as BWO-120, BWO-140, BWO-160, BWO-180, BWO-200, BWO-220, BWO-240, respectively. For comparison, bismuth tungstate was also synthesized at 220 °C using H_2O instead of ethylene glycol as solvent. This sample was assigned as BWO-220H.

Characterization

The crystal structure of the obtained samples was examined on X-ray diffraction (Shimadzu XRD-7000). The surface morphology and microstructure of samples were observed by using scanning electron microscope (FESEM, JSM-7800F) and transmission electronmicroscopy (TEM, JEOL 2100). Nitrogen adsorption–desorption isotherms were collected using AUTOSORB-1 (Quantachrome Instruments) The pore size distribution plots were obtained by the Barret–Joyner–Halenda (BJH) model. UV-vis diffuse reflectance spectra were determined by a UV-Vis spectrophotometer (Shimadzu UV-2550) using an integrating sphere accessory. The photoluminescence (PL) spectra were obtained on fluorescence spectrophotometer with a Xe lamp as light source.

Photocatalysis degradation

The photo-degradation experiments: 25 mg of catalyst powder was dispersed 50 mL 10^{-5} M R6G solution. A 300 W Xe lamp was used as a simulated solar light source. Prior to irradiation, the suspension was kept in the dark under stirring for 60 min to ensure the adsorption/desorption equilibrium. At given time intervals, 2 mL aliquots were collected from the suspension and immediately centrifuged, the concentration of R6G was determined at 526 nm using a UV-vis spectrophotometer.

The transient photocurrent responses experience

The as-prepared samples coated on Fluorine-doped Tin Oxide (FTO) glass with 0.5 cm^2 were used as working electrodes, saturated calomel electrodes (SCE) and platinum sheet were used as the reference electrode and counter electrode, respectively. A 300 W Xe lamp was used as the light source, and the electrochemical tests were carried out at open-circuit voltage in a three-electrode system in 0.1 M Na_2SO_4 solution on electrochemical work station (CHI-660B, CHI Instruments Inc).

Results and discussion

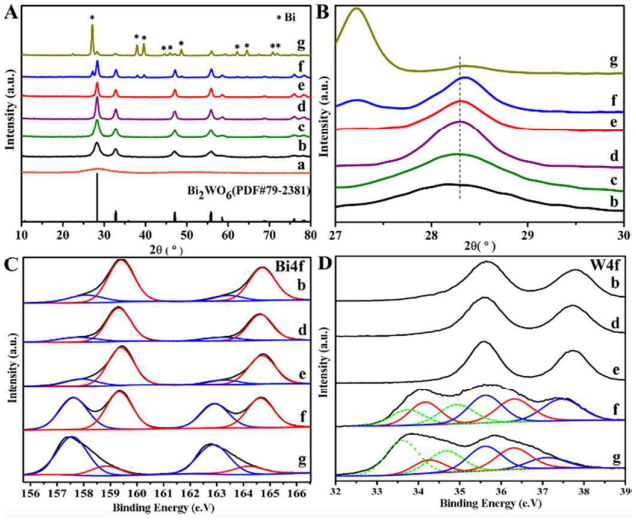

Fig.1 XRD patterns of the samples obtained at different temperature (A) and enlarged view of the XRD patterns of the samples in range of 27.5-29°(B), XPS spectra of Bi4f (C) and W4f (D) for the samples obtained at different temperature. (curve a to g represent the samples obtained at 120, 140, 160, 180, 200, 220 and 240 °C, respectively.)

The influence of reaction temperature on the crystalline phase of the products was first studied by XRD, and the XRD patterns of the obtained samples are illustrated in Fig.1. A broad and poorly defined peaks centered around 28.5° indicated that the sample obtained at 120 °C has a characteristics of amorphous (pattern a in Fig.1A). All of the diffraction peaks of the curve b to e can be indexed to orthorhombic phase of Bi_2WO_6 (Fig 1A) and match very well with the standard XRD pattern (PDF card No. 79-2381). No impurity peaks are observed, indicating that the products obtained at 140, 160, 180 and 200 °C are pure Bi_2WO_6 phase. When the reaction temperature increase to 220 °C, a very weak peak appears at 27.2°, indicating a new phase was formed at higher temperature. Continually increasing the reaction temperature to 240 °C, the peak center at 27.2° becomes very strong and most of the diffraction peaks should be indexed to metal Bi (PDF card No. 85-1330). These results indicated that when the reaction temperature is higher than 220 °C, part of Bi^{3+} was reduced to metal Bi and Bi/bismuth tungstate nanocomposites were obtained. It is noteworthy in Fig.1B that when the temperature is higher than 220 °C, not a new phase, metal Bi appeared in the products, but the peak around 27~29 ° shifted slightly toward a higher 2θ value,

indicating the shrinkage of the unit cell volume of samples due to part of Bi^{3+} ion was reduced to metal Bi.[29] The sample was also prepared at 220 °C using H_2O instead of ethylene glycol as solvent. Its XRD spectrum is shown in Fig S1, which matches very well with that of the pure phase Bi_2WO_6, no any diffraction peaks of metal Bi is observed.

The changes of the chemical state of the elements constituting the temperature-depended products were further investigated by XPS to understand the evolution process of the crystal structure of the relative products. The XPS results recorded from the samples obtained by different reaction temperature are shown in Fig. 1C (Bi 4f) and 1D (W 4f). Clearly all of XPS spectra shown in Fig. 1C. They displayed similar peak positions, which could be deconvoluted into two doublets. One has a Bi $4f_{7/2}$ line at 159.4 and a Bi $4f_{5/2}$ line at 164.7 eV corresponds to the oxidation state of Bi^{3+}. The other one has a Bi $4f_{7/2}$ line at 157.6 and a Bi $4f_{5/2}$ line at 162.9 eV associates to Bi^0.[30] However, it is worth noting that the content of metal Bi in the samples obtained in lower temperature (140~200 °C) is very little, while it became the domain when the temperature is higher than 220 °C, indicating that Bi^{3+} was easily reduced to metallic Bi at higher temperature. The W4f XPS of all samples shown in Fig.1D, when reaction temperature is below 220 °C, only two peaks at 35.57 and 37.74 eV corresponds to $4f_{7/2}$ and $4f_{5/2}$ of the products were observed. However, when the reaction temperature increase to 220 °C, three peaks appeared and shifted to lower energy, which can be deconvoluted into three couples of spin-orbit splitting components (labeled in Fig. 1D (d and e)). The first doublet has a W $4f_{7/2}$ line at 35.56 eV and a W $4f_{5/2}$ line at 37.74 eV, which associated with the oxidation state of W^{6+} presented in all samples. The second doublet has a lower binding energy with W $4f_{7/2}$ line at 34.15 eV and W $4f_{5/2}$ line at 36.35 eV, corresponded to the W^{5+} oxidation state of the relative products. The third doublet has a binding energy with W $4f_{7/2}$ line at 33.62 eV and W $4f_{5/2}$ line at 34.90 eV ascribed to the W^{4+} oxidation state of the products.[31] Further, when the reaction temperature continues increasing to 240 °C, the peaks intensity of W^{4+} and W^{5+} became stronger than that of W^{6+}, which may due to with the reaction temperature increasing, tungsten in products were reduced gradually. Combined with the XRD analysis, it is clearly that at lower temperature (140~200 °C), the as-prepared products are Bi_2WO_6, at 220 °C, the product is $Bi/Bi_{2-x}WO_y$, while at higher temperature (⩾240 °C), metal Bi became the domain product. The XPS spectra of BWO-220H are displayed in Fig.S2, which are agreed well with that of pure phase Bi_2WO_6. This result indicated that ethylene glycol in our experiment is not only a solvent, but a mild reducing agent.

The shape evolution of the synthesized samples under the hydrothermal process was observed by using SEM. Fig.2 clearly displays that the reaction temperature has great impact on the morphology of the as-prepared samples. The sample obtained at 120 °C illustrates irregular spherical agglomerates (Fig. 2A) constructed by small nanoparticles. The product formed at 140 °C grows into well-developed hollow spheres (Fig. 2B), which consisted by very thin nanoplates. When temperature rise to 160 °C (Fig. 2C), partly sphere collapsed and their surface consisted by nanoparticles. However, when the reaction temperature continues increaseing to 180 °C, excessively growth hollow spheres began to collapse. When the reaction temperature further increases to 220 °C, the product has developed to small uniform nanorods, (Fig. 2E). At higher reaction temperature, 240 °C, a lot of small particles gathered together and into microspheres. The above analysis results further confirmed that the reaction temperature has an important influence on the crystal phase and morphology of the products (Fig.2F).

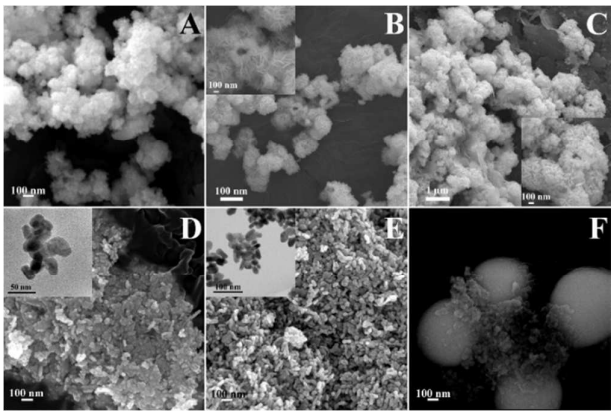

Fig.2 FESEM of the products obtained at different temperature (Fig. 2A to 2F represent the samples obtained at 120, 140, 160, 180, 220 and 240 °C, respectively.) (Inset of 2B and 2D represent the high magnification SEM images of BWO-140 and BWO-160; Inset of 2C and 2E show TEM images of BWO-180 and BWO-220)

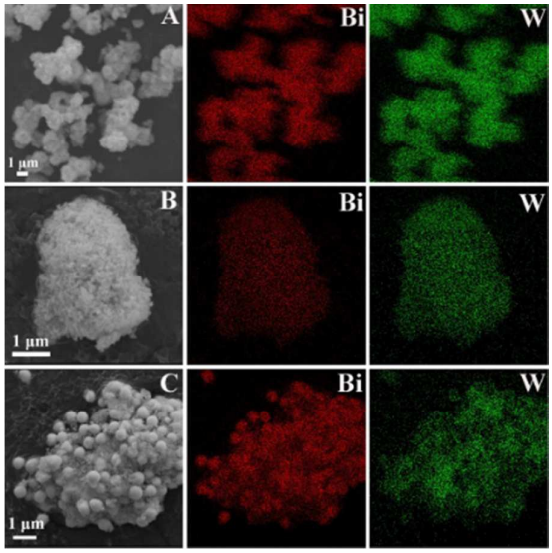

Fig. 3 EDS mapping of the products obtained at 140 (A), 220 (B) and 240 °C (C).

Based on above analysis, when the reaction temperature is higher than 220 °C, not only metal Bi appeared in the products but the morphology of the products has a great change. In

order to examine the dispersion of metal Bi in samples, the energy dispersive spectrometry (EDS) mapping of the products is carried out in our experiment. Interestingly, Bi and W element have a similar graphic pattern just like their electronic images in the samples obtained at 140 and 220 °C, which indicated that these elements are uniformly distributed in the obtained samples. However, combined with its high magnification SEM image (Fig 2F), the spheres appeared in sample prepared at 240 °C are metal Bi, while in the nanoparticles of the sample, Bi and W elements are also uniformly distributed (Fig 3).

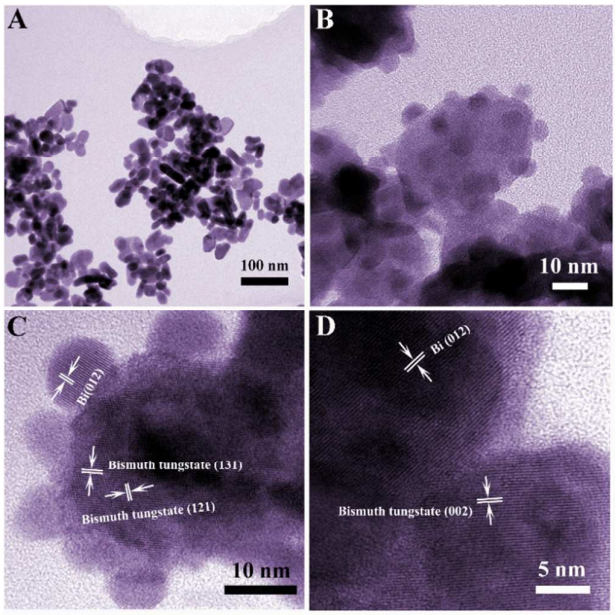

Fig.4 TEM (A) and HRTEM (B) images of product obtained at 220 °C

The morphology and microstructure of the sample obtained at 220 °C were further investigated by using TEM. The panoramic view shown in Fig. 4A indicates that the sample is very small nanorods and dispersed very well. The HRTEM image recorded on the nanorods provided further insight into the microstructures of this material as shown in Figure 4B. Some 5~10 nm nanocrystallites appeared on the surface of the nanorods and distributed uniformly. Clearly resolved lattice fringes shown in Fig. 4C, giving evidence that the nanocrystallites was highly crystallized metal Bi. In Fig.4C, the distance between two fringes is about 0.315 nm and 0.349 nm, which is close to the d spacing of (131) and (121) plane of orthorhombic Bi_2WO_6, respectively and two fringes is about 0.326nm and 0.226 nm, which close to the d spacing of (012) and (110) plane of metal Bi. As clearly shown in Fig.4D, the Bi_2WO_6 closely connect to metal Bi, which could efficiently transfer electrons from Bi_2WO_6 to metal Bi. The results of XRD and HRTEM strongly supports our proposed approach is a desirable process for fabrication of Bi/bismuth tungstate nanocomposites.

It is well known that a small amount of metal nanoparticles modifying could enhance the photocatalytic efficiency of semiconductors through extended electron–hole lifetime due to the photogenerated electrons could be transferred to metal nanoparticles as the composites undergo charge separation.[32, 33] The metal Bi/bismuth tungstate nanocomposites prepared in in situ reaction, in which metallic Bi uniformly dispersed in the samples and closely connected with bismuth tungstate, should be a promising photocatalysts. Hence, in our work, we select three samples prepared at 140, 220, and 240 °C as the representative samples to study the feasibility of them as photocatalysts. As shown in Fig.5, both BWO-140 and BWO-220 can degrade R6G under solar light effectively. Bi/Bismuth tungstate nanocomposite displays the highest photocatalytic activity, which is two times of that pure Bi_2WO_6 and its degradation rate reach to 95.6% in 40 min. However, Bi/Bismuth tungstate (obtained at 240 °C) has negligible photocatalyic activity due to its main component is metal Bi.

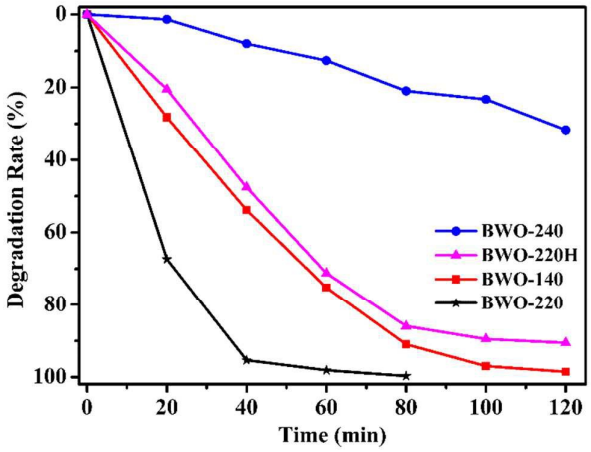

Fig.5 Degradation Rate of R6G in the presence of different photocatalysts

It is generally accepted that the photocatalytic efficiency of a material is closely related to (I) controllable morphology with great specific surface area and suitable pore size distribution, (II) the generation of photogenerated electron-hole pairs and (III) the separation and utilization of the charge carriers.[2] In our work Bismuth tungstate and Bi/Bismuth tungstate could be fabricated by the same hydrothermal process, this offered us a good platform to explore the process-structure-property relationship in photocatalysts synthesis and applications. Hence, the specific surface area, Uv-vis diffuse reflectance spectra, PL spectra and transient photocurrent responses of BWO-140 and BWO-220 were also characterized in detail. The nitrogen adsorption isotherms and pore size distributions of the BWO-140 and BWO-220 are shown in Fig. 6A. The measured specific surface area is 102 and 30 $m^2 g^{-1}$ for BWO-140 and BWO-220, respectively. The hysteresis loop of BWO-140 appears in the low relative pressure (P/P_0) range of 0.45 to 0.9, which might be ascribed to the presence of a mesoporous structure in the interleaving nanoplates or cavities of the hollow spheres, and the hysteresis loop of BWO-220 exhibits in the high relative pressure (P/P_0) range of 0.9 to 1, which might

result from the internanorods space.[34] A greater BET surface area of photocatalysts could be beneficial to achieve better adsorption of dye molecules in aqueous suspension and can supply more surface active sites for the photocatalytic reaction, then in our work, although the specific surface area of BWO-140 is about 3.4 times bigger than that of BWO-220, the photocatalytic activity of BWO-140 is not better than that of BWO-220.

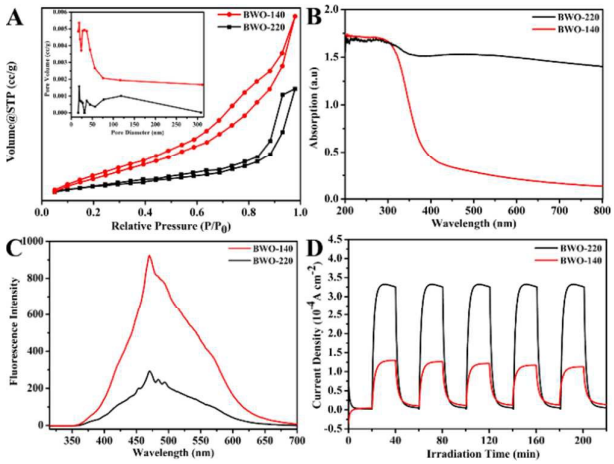

Fig.6 N_2 adsorption–desorption isotherm curves and pore size distribution (A), UV-vis diffuse reflectance spectrum (B), PL spectra (C) and transient photocurrent responses in 0.5M Na_2SO_4 solution under solar light irradiation (D) of BWO-140 and BWO-220.

The Uv-vis diffuse-reflection spectra of the BWO-140 and BWO-220 are displayed in Fig. 6B, the middle wavelength of the absorption edge of both samples are very similar, which indicated that the introduction of metallic Bi does not change the energy band structure of Bi_2WO_6. However, an obvious enhancement in visible light absorption from 420 to 800 nm was observed for the sample introduced metal Bi, which due to the surface plasmon resonance of Bi nanoparticles under solar light irradiation could broaden light absorption range of the material.[35, 36]

It is well known that PL emission has a close relationship with the recombination of excited electrons and holes.[37] As shown in Fig. 6C, the BWO-140 displays a broad emission and a strong emission peak at around 475 nm, which is attributed to the intrinsic luminescence of Bi_2WO_6.[28] Similar emission rang and peak was observed for BWO-220 and consistent with their Uv-vis diffuse reflectance spectra, however, the fluorescence intensity of BWO-220 is much lower than that of BWO-140, which indicated that the introduced metallic Bi can effectively reduce the recombination of electron and hole pairs.

The efficient utilization of photogenerated holes is demonstrated in the photocatalytic oxidation of R6G, improved electrons transfer is verified in the transient photocurrent responses of the BWO-140 and BWO-220 recorded at open-circuit voltage under on-off simulated sunlight irradiation cycles in 0.5 M Na_2SO_4 aqueous solution. As shown in Fig.6D, the BWO-220 exhibits a photocurrent generation of 0.33 mA cm^{-2}, which is greatly enhanced than that of the BWO-140 (0.12 mA cm^{-2}). The improved electrons transfer ability of BWO-220 should ascribed to the tiny Bi nanoparticles formed in in situ reaction process uniformly dispersed on the surface and interior of Bi_2WO_6 nanorods and firmly and effectively contacted with Bi_2WO_6.

Based on above analysis, the reason why BWO-220 with smaller specific surface area showed higher photocatalytic activity compared with BWO-140 is clearly. On the one hand, the surface plasmon resonance of Bi nanoparticles under solar light irradiation could broaden light absorption range of the material; on the other hand, the photo-induced electrons could transfer from the conduction band of $Bi_{2-x}WO_y$ to metal Bi and reduce the quick recombination of photo-generated charge carriers in photocatalytic process.

The durability under repeated photocatalytic process is also an important index to estimate an excellent photocatalyst. The recycling life of BWO-220 for degradation of R6G is shown in Fig.7. No distinct activity decay is observed after five recycling runs.

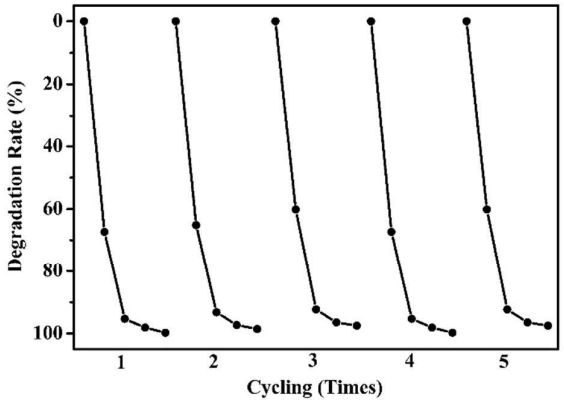

Fig.7 Recycling performance of BWO-220 for R6G degradation in 5 cycles, showing no activity decay

Conclusions

Summary, Bi/bismuth tungstate, a kind of low cost metal-functionalized semiconductor photocatalyst was fabricated by an efficient in situ hydrothermal method. The photocatalytic experimental results indicated that the Bi/bismuth tungstate synthesized at 220 °C exhibited excellent solar-light-driven photocatalytic efficiency for the degradation of Rhodamine 6G (R6G), which may due to the very tiny metal Bi which uniformly distributed in the nanocomposites. It plays an important role in broaden light absorption range, effectively transfer photo generated electron and restrain recombination of electron-hole.

Acknowledgements

This work is financially supported by National Natural Science Foundation of China (21163021); Natural Science Foundation of Chongqing (cstc2013jcyjA5004); Program for Excellent Talents in Chongqing (102060-20600218); Chongqing Key Laboratory for Advanced Materials and Technologies of Clean Energies.

Notes and references

1. R. P. Schwarzenbach, T. Egli, T. B. Hofstetter, U. von Gunten and B. Wehrli, in Annual Review of Environment and Resources, Vol 35, eds. A. Gadgil and D. M. Liverman, Annual Reviews, Palo Alto, 2010, vol. 35, pp. 109-136.
2. N. Zhang, R. Ciriminna, M. Pagliaro and Y. J. Xu, Chem. Soc. Rev., 2014, 43, 5276-5287.
3. B. Muktha, M. H. Priya, G. Madras and T. N. G. Row, J Phys Chem B, 2005, 109, 11442-11449.
4. S. U. Khan, M. Al-Shahry and W. B. Ingler, Science, 2002, 297, 2243-2245.
5. H. Lee and W. Choi, Environ. Sci. Technol., 2002, 36, 3872-3878
6. T. Saison, N. Chemin, C. Chaneac, O. Durupthy, V. Ruaux, L. Mariey, F. Mauge, P. Beaunier and J.-P. Jolivet, Journal of Physical Chemistry C, 2011, 115, 5657-5666.
7. J. W. Tang, Z. G. Zou and J. H. Ye, Catal Lett, 2004, 92, 53-56.
8. L. Zhang, W. Wang, Z. Chen, L. Zhou, H. Xu and W. Zhu, J Mater Chem, 2007, 17, 2526-2532.
9. W. D. Wang, F. Q. Huang and X. P. Lin, Scripta Materialia, 2007, 56, 669-672.
10. M. Shang, W. Wang, J. Ren, S. Sun, L. Wang and L. Zhang, J Mater Chem, 2009, 19, 6213-6218.
11. S.-J. Liu, Y.-F. Hou, S.-L. Zheng, Y. Zhang and Y. Wang, CrystEngComm, 2013, 15, 4124-4130.
12. Y. Zhou, Z. Tian, Z. Zhao, Q. Liu, J. Kou, X. Chen, J. Gao, S. Yan and Z. Zou, ACS applied materials & interfaces, 2011, 3, 3594-3601.
13. X. Wang, L. Chang, J. Wang, N. Song, H. Liu and X. Wan, Appl Surf Sci, 2013, 270, 685-689.
14. X.-F. Cao, L. Zhang, X.-T. Chen and Z.-L. Xue, CrystEngComm, 2011, 13, 306-311.
15. Y. Zhang, N. Zhang, Z.-R. Tang and Y.-J. Xu, Chemical Science, 2013, 4, 1820-1824.
16. Y. Zhang and Y.-J. Xu, RSC Advances, 2014, 4, 2904-2910.
17. X.-J. Dai, Y.-S. Luo, W.-D. Zhang and S.-Y. Fu, Dalton Transactions, 2010, 39, 3426-3432.
18. D. Wu, H. Zhu, C. Zhang and L. Chen, Chem Commun, 2010, 46, 7250-7252.
19. H. Cheng, B. Huang, Y. Liu, Z. Wang, X. Qin, X. Zhang and Y. Dai, Chem Commun, 2012, 48, 9729-9731.
20. L. Zhang, C. Baumanis, L. Robben, T. Kandiel and D. Bahnemann, Small, 2011, 7, 2714-2720.
21. F. Amano, K. Nogami, R. Abe and B. Ohtani, Chem Lett, 2007, 36, 1314-1315.
22. J. Wu, F. Duan, Y. Zheng and Y. Xie, Journal of Physical Chemistry C, 2007, 111, 12866-12871.
23. F. Amano, K. Nogami, R. Abe and B. Ohtani, The Journal of Physical Chemistry C, 2008, 112, 9320-9326.
24. L. Xu, X. Yang, Z. Zhai and W. Hou, CrystEngComm, 2011, 13, 7267-7275.
25. D. He, L. Wang, H. Li, T. Yan, D. Wang and T. Xie, CrystEngComm, 2011, 13, 4053-4059.
26. Z. Chen, L. Qian, J. Zhu, Y. Yuan and X. Qian, CrystEngComm, 2010, 12, 2100-2106.
27. D. Ma, S. Huang, W. Chen, S. Hu, F. Shi and K. Fan, The Journal of Physical Chemistry C, 2009, 113, 4369-4374.
28. Y. Li, J. Liu, X. Huang and G. Li, Crystal growth & design, 2007, 7, 1350-1355.
29. M.-S. Gui and W.-D. Zhang, Nanotechnology, 2011, 22, 265601.
30. S. Vinu, P. Sarun, A. Biju, R. Shabna, P. Guruswamy and U. Syamaprasad, Supercond Sci Technol, 2008, 21, 045001.
31. J. Medina-Ramos, J. L. DiMeglio and J. Rosenthal, J Am Chem Soc, 2014, 136, 8361-8367.
32. S. Jeon and K. Yong, Nanotechnology, 2007, 18, 245602.
33. M. Ni, M. K. Leung, D. Y. Leung and K. Sumathy, Renewable and Sustainable Energy Reviews, 2007, 11, 401-425.
34. T. Hirakawa and P. V. Kamat, J Am Chem Soc, 2005, 127, 3928-3934.
35. Y. Tao, H. Kanoh, L. Abrams and K. Kaneko, Chem Rev, 2006, 106, 896-910.
36. D. Wang, G. Xue, Y. Zhen, F. Fu and D. Li, J Mater Chem, 2012, 22, 4751-4758.
37. Y. Wang, B. H. Hong and K. S. Kim, The Journal of Physical Chemistry B, 2005, 109, 7067-7072.
38. X. Li, F. Li, C. Yang and W. Ge, Journal of Photochemistry and Photobiology A: Chemistry, 2001, 141, 209-217.